



## Evaluating the effects of surface properties on methane retrievals using a synthetic airborne visible/infrared imaging spectrometer next generation (AVIRIS-NG) image



Alana K. Ayasse<sup>a,\*</sup>, Andrew K. Thorpe<sup>b</sup>, Dar A. Roberts<sup>a</sup>, Christopher C. Funk<sup>c</sup>, Philip E. Dennison<sup>d</sup>, Christian Frankenberg<sup>e,b</sup>, Andrea Steffke<sup>f</sup>, Andrew D. Aubrey<sup>g,b</sup>

<sup>a</sup> Department of Geography, University of California, Santa Barbara, Santa Barbara, CA, United States of America

<sup>b</sup> Jet Propulsion Laboratory, California Institute of Technology, Pasadena, CA, United States of America

<sup>c</sup> U.S. Geological Survey and Climate Hazards Group, Department of Geography, University of California, Santa Barbara, Santa Barbara, CA, United States of America

<sup>d</sup> Department of Geography, University of Utah, Salt Lake City, UT, United States of America

<sup>e</sup> California Institute of Technology, Division of Geological and Planetary Sciences, Pasadena, CA, United States of America

<sup>f</sup> Chevron Energy Technology Company, San Ramon, CA, United States of America

<sup>g</sup> SeekOps Inc., Pasadena, CA, United States of America

### ARTICLE INFO

#### Keywords:

Methane

CH<sub>4</sub>

Airborne visible/infrared imaging spectrometer

next generation

AVIRIS-NG

Synthetic images

Sensitivity

Albedo

Land cover

Remote sensing

### ABSTRACT

Atmospheric methane has been increasing since the beginning of the industrial era due to anthropogenic emissions. Methane has many sources, both natural and anthropogenic, and there continues to be considerable uncertainty regarding the contribution of each source to the total methane budget. Thus, remote sensing techniques for monitoring and measuring methane emissions are of increasing interest. Recently, the Airborne Visible-Infrared Imaging Spectrometer - Next Generation (AVIRIS-NG) has proven to be a valuable instrument for quantitative mapping of methane plumes. Despite this success, uncertainties remain regarding the sensitivity of the retrieval algorithms, including the influence of albedo and the impact of surfaces that may cause spurious signals. To explore these sensitivities, we applied the Iterative Maximum a Posterior Differential Optical Absorption Spectroscopy (IMAP-DOAS) methane retrieval algorithm to synthetic reflected radiances with variable methane concentrations, albedo, surface cover, and aerosols. This allowed for characterizing retrieval performance, including potential sensitivity to variable surfaces, low albedo surfaces, and surfaces known to cause spurious signals. We found that dark surfaces (below  $0.10 \mu\text{Wcm}^{-2}\text{nm}^{-1}\text{sr}^{-1}$  at 2139 nm), such as water and green vegetation, and materials with absorption features in the 2200–2400 nm range caused higher errors in retrieval results. We also found that aerosols have little influence on retrievals in the SWIR. Results from the synthetic scene are consistent with those observed in IMAP-DOAS retrievals for real AVIRIS-NG scenes containing methane plumes from a waste dairy lagoon and coal mine ventilation shafts. Understanding the effect of surface properties on methane retrievals is important given the increased use of AVIRIS-NG to map gas plumes from a diversity of sources over variable landscapes.

### 1. Introduction

Methane (CH<sub>4</sub>) is a potent greenhouse gas that contributes significantly to global climate change. Methane is estimated to be responsible for about 20% of the total global warming induced by anthropogenic greenhouse gases (Kirschke et al., 2013) and abundances have been increasing since the industrial revolution (Ciais et al., 2013). However, from 1999 to 2006 the growth rate stagnated only to rise again starting in 2007 (IPCC, 2016; Nisbet et al., 2014). The cause of this stagnation and subsequent rise is still debated. Some argue that the

increase in methane is due to the natural gas industry while others argue it is due to increased emissions from wetlands (Nisbet et al., 2016; Schaefer et al., 2016; Schwietzke et al., 2016). Other studies point to changes in the methane lifetime (Rigby et al., 2017; Turner et al., 2017). Regardless of cause, the recent unexpected rise in methane reflects our uncertainty regarding the contribution of various sources to the total methane budget. In addition, recent increases in atmospheric methane have revived concern about its relative contribution to global warming, which has resulted in some states, such as California, enacting new regulations to curb emissions (SB-1383, Lara, 2016; AB-

\* Corresponding author.

E-mail address: [alanaayasse@geog.ucsb.edu](mailto:alanaayasse@geog.ucsb.edu) (A.K. Ayasse).

1496, [Thurmond, 2015](#)). These policy measures underscore the importance of unraveling sectoral contributions through deployment of effective techniques for monitoring and quantifying methane emissions.

Using remote sensing to study greenhouse gases, such as methane, has gained prominence over the last decade ([Jacob et al., 2016](#)). There have been a variety of instruments launched into space with the goal of observing methane and other greenhouse gases. The Atmospheric Infrared Sounder (AIRS), the Scanning Imaging Absorption Spectrometer for Atmospheric Chartography (SCIAMACHY), and the Greenhouse gases Observing SATellite (GOSAT) are three such examples ([Frankenberg et al., 2011](#); [Strow et al., 2003](#); [Yokota et al., 2009](#)). These sensors generate global maps of gas concentrations with coarse spatial resolutions on the order of kilometers. AIRS, SCIAMACHY, and GOSAT have greatly increased our understanding of global methane distribution and quantity, but lack the spatial resolution to directly attribute observed emissions to individual sources. Finer spatial resolution sensors are necessary to improve sensitivity to local emissions sources. For example, the 30 m pixel resolution of the Hyperion imaging spectrometer enabled the space-based detection of a methane plume from Aliso Canyon ([Thompson et al., 2016](#)). However, the Aliso Canyon plume was anomalously large and Hyperion was not well suited for methane detection given an aged focal plane at the time of detection and low signal-to-noise ratio in wavelength regions capturing methane absorption ([Green et al., 2003](#)).

In addition to space-based observations, airborne observations have also been used to detect and measure methane. Airborne remote sensing has fine spatial resolution and is well suited to resolving individual sources, although these retrievals are limited in time. Current airborne sensors used to measure methane emissions include the Methane Airborne Mapper (MAMAP), a non-imaging spectrometer specifically designed to map methane and carbon dioxide ([Gerilowski et al., 2011](#)). This sensor was able to obtain flux estimates from point sources such as landfills and coal mine ventilation shafts ([Krautwurst et al., 2017](#); [Kriings et al., 2013](#)). MAMAP and other similar sensors are able to make very accurate column concentration estimates but must fly many downwind transects in order to map a full plume. This makes detection of emissions from unknown sources difficult, and these sensors are best suited for studying known methane sources. More recently, imaging spectrometers have been used to map methane. Thermal imaging spectrometers such as Mako and the Hyperspectral Thermal Emission Spectrometer (HyTES) have successfully mapped methane plumes from multiple sources ([Hulley et al., 2016](#); [Tratt et al., 2014](#)). However, the sensitivity of these sensors to emissions near the ground depends on the thermal contrast between the ground and atmosphere and decreases as flight altitude increase, which in turn limits ground coverage.

The Airborne Visible and Infrared Imaging Spectrometer (AVIRIS) and the Next Generation instrument (AVIRIS-NG) are imaging spectrometers that measure reflected solar radiation in the visible and shortwave infrared (VSWIR) and have also been used to map methane emissions ([Frankenberg et al., 2016](#); [Roberts et al., 2010](#); [Thompson et al., 2015](#); [Thorpe et al., 2013, 2017](#)). AVIRIS measures a spectral range between 400 and 2500 nm and has a 10 nm spectral sampling ([Green et al., 1998](#)) while AVIRIS-NG measures the same spectral range with 5 nm spectral sampling and improved signal to noise ratio (SNR)

([Hamlin et al., 2011](#)). AVIRIS-NG has a 34° field of view with a 1 mrad instantaneous field of view that results in spatial resolutions that typically range between 1 and 8 m depending on the flight altitude. These sensors were not originally designed to map greenhouse gases but their sensitivity to gas absorption features between 900 nm and 2500 nm has allowed for detection and quantitative mapping of methane, carbon dioxide, and water vapor ([Bradley et al., 2011](#); [Dennison et al., 2013](#); [Gao and Goetz, 1990](#); [Roberts et al., 2010](#); [Thorpe et al., 2017](#)). Recently, quantitative retrievals have been developed to estimate column concentrations of methane from AVIRIS-NG data ([Thompson et al., 2015](#); [Thorpe et al., 2014](#); [Thorpe et al., 2017](#)). For example, the Iterative Maximum a Posterior Differential Optical Absorption Spectroscopy algorithm (IMAP-DOAS; [Frankenberg et al., 2004](#)) was adapted for AVIRIS-NG ([Thorpe et al., 2017](#)). Success using AVIRIS-NG for methane mapping has prompted multiple flight campaigns in the Western United States focused on mapping methane emissions from the energy sector ([Thompson et al., 2015](#); [Frankenberg et al., 2016](#); [Thorpe et al., 2017](#)).

Although AVIRIS-NG has been used successfully to map methane plumes, there are still uncertainties regarding the sensitivity of the retrieval algorithms, including the influence of albedo on results and the impact of surfaces that can cause spurious signals. Low albedo surfaces reduce the observable difference in reflected radiance between a background methane concentrations and enhanced concentrations. At the 5 nm spectral sampling of AVIRIS-NG, surfaces with absorption features in the shortwave infrared can mimic the absorptions caused by methane. In this study, we apply the IMAP-DOAS algorithm to a synthetic image with variable methane concentrations, surfaces, and albedo. In an observed AVIRIS-NG scene we cannot control the exact column concentration of a gas, but synthetic radiances based on accurate radiative transfer modeling allows us to control these values and therefore test the accuracy of the algorithms used to estimate the gas concentrations ([Dennison et al., 2013](#); [Guanter et al., 2009](#); [M. Zhang et al., 2017](#)). In addition, the land cover properties, such as albedo and surface type, can be controlled, allowing us to test the sensitivity of the algorithms to these factors. The ability to manipulate these parameters allows us to quantify how the retrieval algorithm is impacted by variations in albedo, surface type, and specific surfaces known to cause spurious signals in order to improve our understanding of retrieval results. In this study, we will first create a synthetic image, run the IMAP-DOAS retrievals algorithm on the synthetic image, and then compare the retrieved CH<sub>4</sub> values to the known values.

## 2. Methods

The general method for this study is to create a synthetic image and to run the IMAP-DOAS algorithm on the synthetic image. [Fig. 1](#) summarizes the workflow for creating the synthetic image and the steps to achieve the results discussed subsequently. Details on the synthetic image and IMAP-DOAS algorithm are discussed below.

### 2.1. Synthetic image

The synthetic image used in this study consists of three main

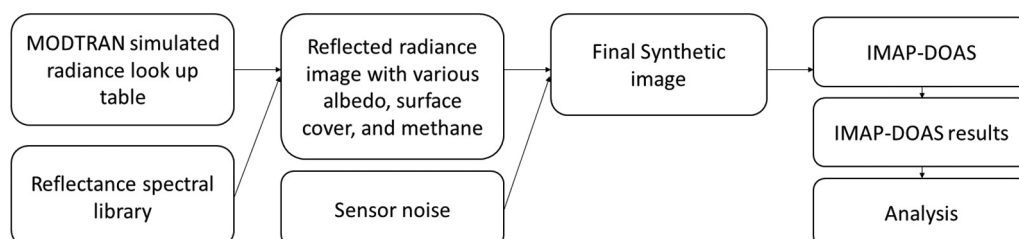


Fig. 1. Workflow framework for the study.

components; it has 30 different surface types modeled at 50 surface albedos and 25 different methane concentrations. MODTRAN 5.3, a radiative transfer model, was used to simulate reflected solar radiance spectra for the synthetic image (Berk et al., 2005). MODTRAN is commonly used to create lookup tables for many atmospheric correction algorithms including ACORN (Kruse, 2004; Miller, 2002) FLAASH (Adler-Golden et al., 1999; Matthew et al., 2002), and ATCOR (Gao et al., 2009; Richter, 1996). It has also been used in a similar way to retrieve water vapor and carbon dioxide from AVIRIS images (Gao and Goetz, 1990). We generated a radiance look up table that consisted of radiance files with 1000 brightness levels and 25 methane concentrations. The methane concentration within the lowest 1 km of the atmosphere, intended to simulate a methane plume or local emission source, ranged from 0 ppm to 12.5 ppm above a background of 1.864 ppm with a 0.5 ppm step (Fig. 3). The MODTRAN atmospheric profiles used to generate these synthetic radiances were modified to match profiles used in the IMAP-DOAS retrieval (see Section 2.2). Assuming a 4 km sensor height and a nadir view zenith angle, two-way transmittance (upwelling and downwelling) was calculated for the atmospheric layers below the sensor, including the 1 km layer with variable methane concentrations (Fig. 2). The solar reflected radiance was then convolved to the AVIRIS-NG wavelengths using the AVIRIS-NG sensor response function; this produced 432 bands with approximately 5 nm full width half maximum.

The additional atmospheric and geometric variables included in the model were held constant and are listed in Table 1. These variables reflect typical conditions under which AVIRIS-NG data are collected. The sensor height in the original studies using AVIRIS Classic to detect methane was 8.95 km (Bradley et al., 2011; Roberts et al., 2010). Recent AVIRIS-NG flight campaigns that have targeted methane emissions had sensor heights ranging from 0.43 to 3.8 km with the average around 3 km (Duren et al., 2017; Thorpe et al., 2016a, 2016b). In this study, a height of 4 km was chosen to reflect the upper limit of typical AVIRIS-NG flights for methane mapping. Given this sensor height, methane concentrations were calculated in units of mixing ratio-path length (ppm-m) for the 0 to 4 km layer to permit direct comparison

**Table 1**

AVIRIS-NG inputs for the MODTRAN simulation. The attributes are the environmental factors affecting the radiative transfer model and the values are the modeled values. All attributes remain constant except for albedo and methane.

Attribute	Values
Sensor height	4 km above sea level
Wavelengths	350–2500 nm
Carbon dioxide	405 ppm
Water vapor	1.535 cm
Visibility	30 km
View zenith angle	0 degrees
Latitude	34.1
Longitude	−118.4
Day of Year (Julian Day)	262
Time (UTC)	21.30
Solar Zenith Angle	29.77 degrees
Methane (in 1 km layer)	1.864 ppm–14.364 ppm

between the modeled concentrations in the synthetic image and the IMAP-DOAS retrieval results. The volume mixing ratios (VMRs) generated by MODTRAN for each kilometer layer of the 0–4 km layer were multiplied by 1000 m and summed. The lowest methane concentration modeled in the image is 6264 ppm-m and the highest concentration, with a 12.5 ppm enhancement above background, is 18,764 ppm-m. The background carbon dioxide, water vapor, location, date, and time of day all represent typical conditions for AVIRIS-NG data collection. The MODTRAN visibility was set at 30 km for a rural atmosphere, including scattering components comprised of 70% ammonium, calcium sulfate, and other organic compounds and 30% dust like aerosols (Carr, 2005). Additional testing was done to determine that a single visibility was sufficient.

Scattering from aerosols in the atmosphere is hypothesized to have a minimal impact on AVIRIS-NG methane retrievals due to the small amount of scattering in the shortwave infrared (SWIR; 1100 to 3000 nm; Dennison et al., 2013). In order to test this assumption and to be confident that the use of a single 30 km visibility was sufficient, we created a small synthetic image with all of the same attributes described below but with a 5 km visibility for a rural atmosphere. The 30 km visibility atmosphere has a total column extinction coefficient of 0.177 and the 5 km visibility atmosphere has a 1.082 total column extinction coefficient (MODTRAN normalizes the extinction coefficient to 1 at 550 nm). The 5 km visibility value was chosen because it is an extreme example, therefore any effects from aerosols should be apparent based on the differences between 5 and 30 km visibility. This image had the same variable land cover and albedo (described below) but only had three methane concentration (1.864 ppm, 2.864 ppm, 9.864 ppm). The IMAP-DOAS algorithm was run on this image in the same way described later (see Section 2.2) and the results are reported in Section 3.1.

The spectra selected for this study represent surface types common in both natural and urban areas. The surfaces include common cover types imaged by AVIRIS-NG and surfaces hypothesized to be challenging for methane mapping. The majority of the surface spectra used to construct the synthetic image were derived from a spectral library originally developed by Roberts et al. (2017) that consists of spectra representing urban and natural environments in Southern California. The spectra were originally collected from a combination of Analytical Spectral Device (ASD) measurements and AVIRIS Classic data. Two additional spectra were obtained from other sources, a calcite spectrum from the US Geological Survey and oil coated vegetation from an AVIRIS Classic image of the Louisiana coastline following the Deep Water Horizon oil spill (Kokaly et al., 2013). The spectral library was convolved and resampled to AVIRIS-NG band centers and full-width half maxima. The surface types are broken up into eight main categories: Green Vegetation (GV), Non-Photosynthetic Vegetation (NPV), soil (or bare soil), water, paved material, roofs, rocks, and “confusers”.

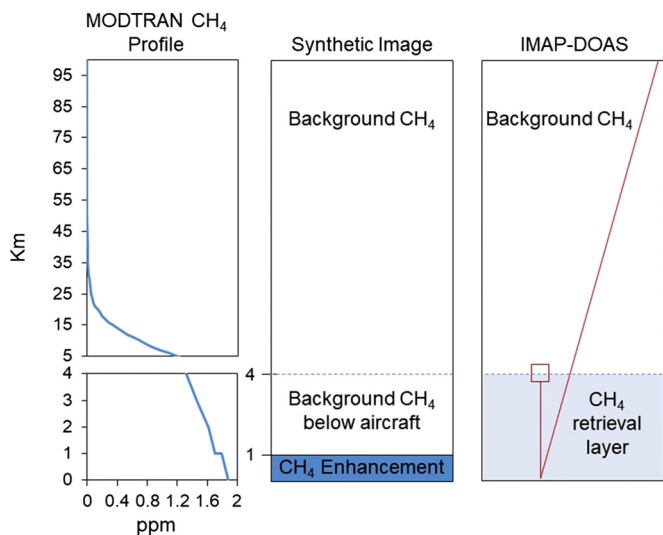


**Fig. 2.** The left panel is the methane profile modeled by MODTRAN for an atmosphere with no methane enhancement. The bottom 0–4 km layer is plotted on a different scale than the 5–100 km layer. The middle panel is a schematic of how the synthetic image models methane in the atmosphere. The far right panel shows IMAP-DOAS retrieval layers, and the light blue layer is below the sensor where the algorithm allows for methane perturbation. For the IMAP-DOAS retrieval, the methane profile above the sensor (white layer) remains constant. The red square represents the sensor and the red line represents transmittance path from the sun to the sensor. (For interpretation of the references to colour in this figure legend, the reader is referred to the web version of this article.)

**Table 2**  
The surface type and spectra used to create the synthetic image.

Land cover class	Surface name
Confusers	Oil coated vegetation
	White painted commercial roof 1 (WPCR1)
	Calcite
	Plastic covered crops
	White painted commercial roof 2 (WPCR2)
	White painted commercial roof 3 (WPCR3)
Green Vegetation (GV)	Ceanothus (CEME)
	Wetland Vegetation (MARSH)
	Coyote brush (BAPI)
	Willow (SASP)
	Golf course grass
Water	Palm tree
	Hope Lake
Rock	Ocean water (glint)
	Rock
Non-Photosynthetic Vegetation (NPV)	Dead grass
	Evergreen bark
	Bark
	Needle litter
Paved Surfaces	Airport asphalt
	Concrete bridge
	Concrete parking structure 1
	Concrete parking structure 2
	Tennis court
Roof	Asphalt & gravel roof
	Red tile roof
Soil	Soil 1
	Soil 2
	Soil 3
	Soil 4

Previous studies have hypothesized that surfaces with strong hydrocarbon absorptions can be potential confusers (Thorpe et al., 2013), therefore the spectra in the confuser class were selected because they contained hydrocarbons or similar SWIR absorptions, which might interfere with the methane absorption features. This class consists of materials such as white painted commercial roof (WPCR), calcite, plastic covered vegetation (greenhouse), and oil-coated vegetation. The individual spectra used in all the classes are listed below in Table 2.

The spectral library reflectance data were converted to radiance using the aforementioned look up table. For each wavelength of each reflectance spectrum, the reflectance value was matched with the closest simulated reflectance value for a specified methane concentration (Dennison et al., 2013). The corresponding radiance from the lookup table was then extracted, and the process was repeated for the next wavelength. This was then repeated for every methane concentration and every reflectance spectrum, to create a synthetic image of radiance spectra with known atmospheric parameters.

The layout of the synthetic image is such that there are 30 “boxes” on the grid, and each box represents a single background spectrum. The bottom half of the box has methane concentrations grading from 0 to 12.5 ppm above background in 25 steps. The top half of the box uses background methane throughout the entire atmosphere. The reflectance of the background spectrum varied from 2% on the left to 52% on the right. Fig. 3 depicts how the surface type, methane, and albedo vary across the image. The gridded layout allowed for easy visual analysis of the performance of IMAP-DOAS algorithm. A noise component aimed at mimicking sensor noise was added using noise equivalent delta radiance (NEdL) to parameterize random noise (Dennison et al., 2013). NEdL is the minimum change in radiance distinguishable from sensor noise and varies by wavelength and radiance level. For each pixel at each wavelength, the NEdL value is calculated by using the original radiance value and NEdL coefficients that were calculated by Dennison et al. (2013). A random number between 0 and

2 was generated and multiplied by the NEdL value so that different amounts of noise were added to each pixel with the average amount being the original NEdL value. The result was then added to the original radiance value. The purpose of varying NEdL was not to simulate the radiance distribution of sensor noise, but rather to create random but true to life variation in each pixel. The total size of the image was 500 by 612 pixels.

## 2.2. The IMAP-DOAS retrieval algorithm

Based on the Beer-Lambert law, Differential Optical Absorption Spectroscopy (DOAS) describes the relationship between incident intensity for the vertical column and measured intensity after passing through a light path containing an absorber (DOAS, Platt, 1994). The IMAP-DOAS retrieval incorporates optimal estimation theory to adjust the column densities of gases until there is optimal agreement between the measured and modeled radiances (Frankenberg et al., 2005) and has been modified for use with AVIRIS-NG (Thorpe et al., 2017). For this study, IMAP-DOAS was setup to model reflected solar radiation using a two layer model. Above the aircraft, the vertical optical densities were combined with an air mass factor (AMF) calculated to account for one-way transmission. Below the aircraft, vertical optical densities were also combined and an AMF calculated to account for two-way transmission (Fig. 2). Atmospheric profiles from the LOW-TRAN/MODTRAN U.S. standard atmosphere (Kneizys et al., 1996) were updated to reflect background concentrations, including 1.864 ppm methane near the surface and volume mixing ratios (VMR) that decreased with altitude. These atmospheric profiles and spectral parameters for methane, water vapor, and nitrous oxide from the HITRAN database (Rothman et al., 2009) were used to calculate vertical optical densities.

Methane retrievals were performed between 2215 and 2410 nm and included fits for the additional absorbing species of water vapor and nitrous oxide. The resulting state vector ( $\vec{x}_n$ ) has six entries (three gases for two atmospheric layers). Modeled radiance was calculated for each wavelength with a forward radiative transfer model using the following equation:

$$\vec{F}^{hr}(\vec{x}_i) = \vec{I}_0^{hr} * \exp\left(-\sum_{n=1}^6 \vec{A}_n \cdot \vec{\tau}_n^{ref} \cdot \vec{x}_{n,i}\right) * \sum_{i=0}^k a_k \lambda^k. \quad (1)$$

where  $\vec{F}^{hr}(\vec{x}_i)$  is the forward modeled radiance (high spectral resolution) at the  $i$ -th iteration of the state vector,  $\vec{I}_0^{hr}$  is the incident intensity (solar transmission spectrum),  $\vec{A}_n$  is the AMF for each  $n$  number of atmospheric state vector elements (6 rows, specified for each of the 2 layers and repeated for each gas),  $\vec{\tau}_n^{ref}$  is the reference total optical density for each  $n$  number of atmospheric state vector elements (including optical densities of methane, water vapor, and nitrous oxide),  $\vec{x}_{n,i}$  is the gas related state vector at the  $i$ -th iteration (gas scaling factor), which scales the prior optical densities of methane, water vapor, and nitrous oxide in each  $n$  layer (6 rows).  $a_k$  are polynomial coefficients to account for broadband variability in surface albedo. The high resolution modeled radiance  $\vec{F}^{hr}$  is then convolved with the ILS and sampled to the center wavelengths of each AVIRIS-NG spectral band. This results in a low resolution modeled radiance at the  $i$ -th iteration of the state vector ( $\vec{F}^{lr}(\vec{x}_i)$ ), calculated using a known  $\vec{\tau}_n^{ref}$  scaled by  $\vec{x}_{n,i}$ .

The IMAP-DOAS algorithm was run using the same parameters used to generate the synthetic image, including the sensor height, location, date, time, and solar zenith angle (Table 1). In this study, the IMAP-DOAS algorithm assumed background concentrations above the aircraft and perturbed the absorbing species in the lowest layer of the model (from 0 to 4 km). The resulting gas state vector for the lowest layer of the model at the last iteration (gas scaling factor, see  $\vec{x}_{n,i}$ ) was then multiplied by the product of the VMR for the lowest layer of the

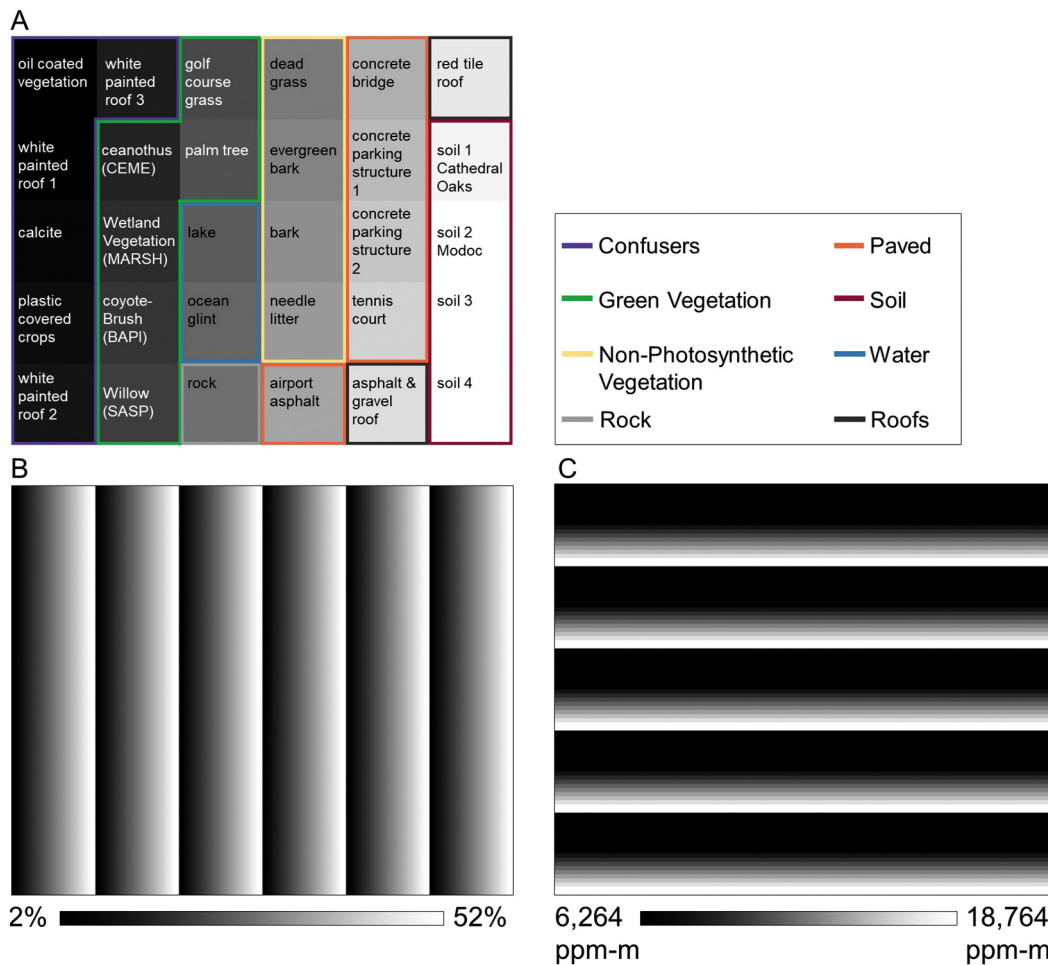


**Fig. 3.** The organization of the synthetic image. A. The location of the surface types in the synthetic image. B. The modeled albedo levels for each background spectrum varied from 2% on the left to 52% on the right. C. The modeled methane concentrations in ppm-m for the atmosphere between 0 and 4 km.

reference atmosphere and the distance between the aircraft and the ground, resulting in gas concentrations in units of ppm-m. Therefore, IMAP-DOAS retrievals reflect the methane concentrations present in the atmospheric subcolumn beneath the aircraft (from 0 to 4 km). Additional details on the IMAP-DOAS retrieval can be found in Thorpe et al. (2014, 2017).

### 3. Results

#### 3.1. Aerosol scattering

We first tested the effects of aerosol scattering on the IMAP-DOAS results. We found that the differences between the modeled methane and IMAP-DOAS retrieved methane is much larger than the differences between the 5 and 30 km visibility (Fig. 4A), indicating that more error is associated with surface type or albedo than visibility. Fig. 4B shows that the distribution of the difference for 5 km and 30 km is very similar with a slight offset between the peaks, corresponding to a mean difference of 1559.9 ppm-m for the 5 km visibility and 1712.39 ppm-m for the 30 km visibility. In addition to the differences between the 5 and 30 km histograms being relatively minor, 5 km visibility is an extremely low visibility and in practice there would be smaller differences in retrieved concentrations across a more realistic range in visibilities.

#### 3.2. IMAP-DOAS

The IMAP-DOAS algorithm was successful in retrieving the modeled

methane enhancement in the synthetic image (Fig. 5). In addition, the pattern and values of retrieved methane enhancement was consistent with the methane enhancement modeled in the synthetic image. Initial visual analysis indicates that the IMAP-DOAS retrieved methane concentration ranged from between 5000 and 6000 ppm-m and then gradually increased until it reached the 18,000 to 20,000 range (Fig. 5). The most notable exception was the Hope Lake box (the box displayed white). This water spectrum had very low reflectance between 2215 and 2410 nm, resulting in no ability to retrieve or detect methane using IMAP-DOAS.

Fig. 6 shows the correlation between the methane concentration from the synthetic image and the IMAP-DOAS retrieved concentrations for the entire image except pixels using the Hope Lake spectrum. The best fit trend was close to the 1:1 line, however IMAP-DOAS underestimated the modeled concentrations by an average error of  $385.11 \pm 1568.33$  ppm-m (Table 3) and the RMSE for the entire image was 1614.92 ppm-m. These results incorporate all land cover types except the lake water and include confusers. The average RMSE dropped to 862.75 ppm-m and the average error dropped to an overestimate of  $5.93 \pm 862.73$  ppm-m when the confuser and Hope Lake background spectra were excluded. When we organize the results by land cover class, it becomes clear that each class responds differently, and a few classes are primarily responsible for the spread in the data. Fig. 7 plots the IMAP-DOAS results against the modeled methane for eight different land cover classes (rock is combined with the soils and lake water and sun glint are separated) and Table 3 summarizes the mean error for each land cover class. We found roofs, soil, NPV, and sun

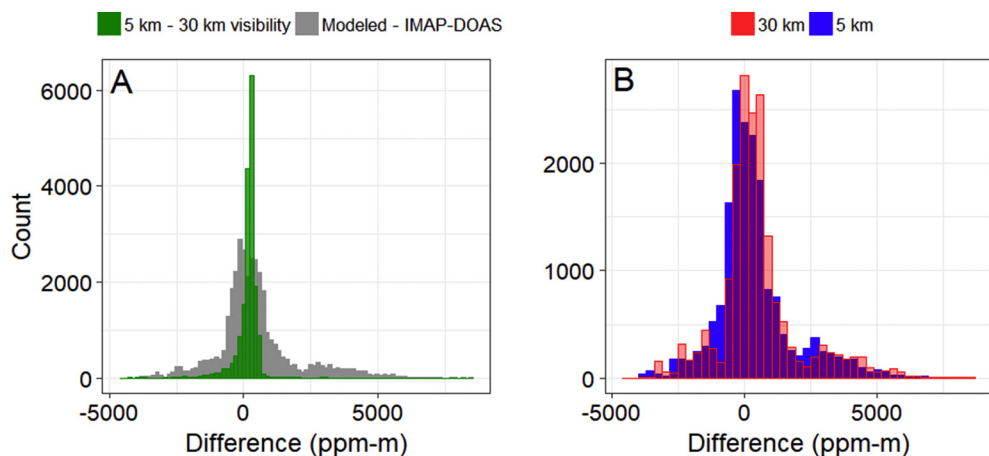


Fig. 4. A) The green histogram shows the difference in the retrieved IMAP-DOAS results for the 5 km visibility and the 30 km visibility. The gray histogram is the difference between the methane modeled in the synthetic image and the methane retrieved by IMAP-DOAS for both visibilities. B) The blue histogram is the difference between the methane modeled in the synthetic image and the IMAP-DOAS results for the 5 km visibility atmosphere. The red histogram is the difference between the methane modeled in the synthetic image and the IMAP-DOAS results for the 30 km visibility atmosphere. (For interpretation of the references to colour in this figure legend, the reader is referred to the web version of this article.)

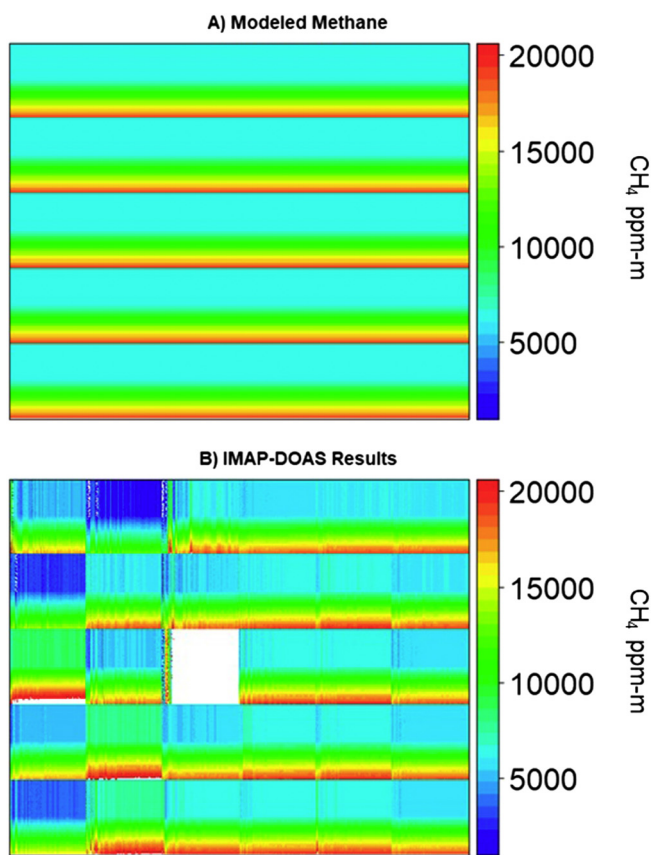


Fig. 5. The methane concentration in ppm-m modeled by A) MODTRAN, and B) retrieved by IMAP-DOAS. Scaling in the two plots is the same, with results outside of the displayed range shown in white. See Fig. 3 for the configuration of the synthetic image.

glint all had good agreement and low spread (Fig. 7, Table 3). The lake water, green vegetation, and confusers all had relatively poor agreement and larger spread (Fig. 7, Table 3).

### 3.3. Surface type

In addition to looking at the correlation between IMAP-DOAS retrieved concentration and synthetic image concentration, we also looked at the per-pixel error. Fig. 8 shows the error between IMAP-DOAS retrieved and synthetic image concentrations (synthetic image minus IMAP-DOAS). In total, 90% of the error (excluding Hope Lake) fell between -1941.65 and 3793.06 ppm-m. Excluding the confusers as

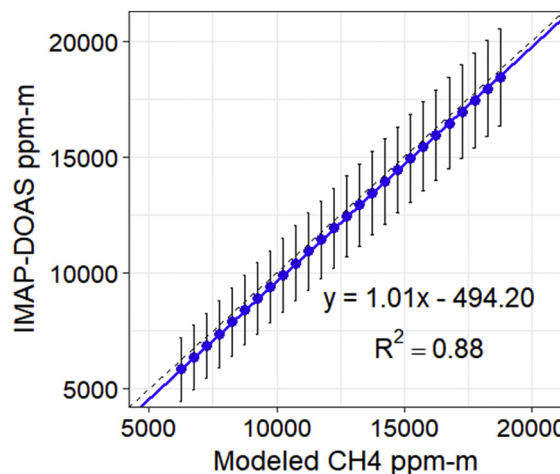


Fig. 6. The mean IMAP-DOAS retrieved concentration for each synthetic image concentration, plotted against the image concentration for all pixels except Hope Lake. The error bars represent one standard deviation. The dotted line represents the one to one line and the blue solid line is the linear fit. The linear model has a slope of 1.01, an intercept of -494.2, and an R-squared of 0.88. (For interpretation of the references to colour in this figure legend, the reader is referred to the web version of this article.)

Table 3

The mean error between the synthetic image and retrieved IMAP-DOAS methane concentrations. The mean error is the average of the residuals between the known methane concentrations from the synthetic image and IMAP-DOAS retrieved methane concentrations (negative means are overestimations and positive means are underestimations).

Land cover class	Mean error ppm-m
Confusers	1884.10 ± 2490.45
Paved	-243.92 ± 382.39
GV	-62.51 ± 1466.72
Soil	372.45 ± 307.40
Lake Water (Hope Lake)	-32,757.44 ± 16,661.13
NPV	22.44 ± 462.67
Sun Glint	645.49 ± 310.57
Roofs	-168.62 ± 428.80
All (except Hope Lake)	385.11 ± 1568.33
All (except Hope Lake and Confusers)	-5.93 ± 862.73

well, the 90% range decreased from the afore mentioned range to -1609.96 ppm-m to 998.36 ppm-m. We observed a few distinct patterns in error (Figs. 8 and 9). First, the error seems to be related to individual surface types because different background spectra boxes have distinctive error patterns. Some surface types (Lake water, white

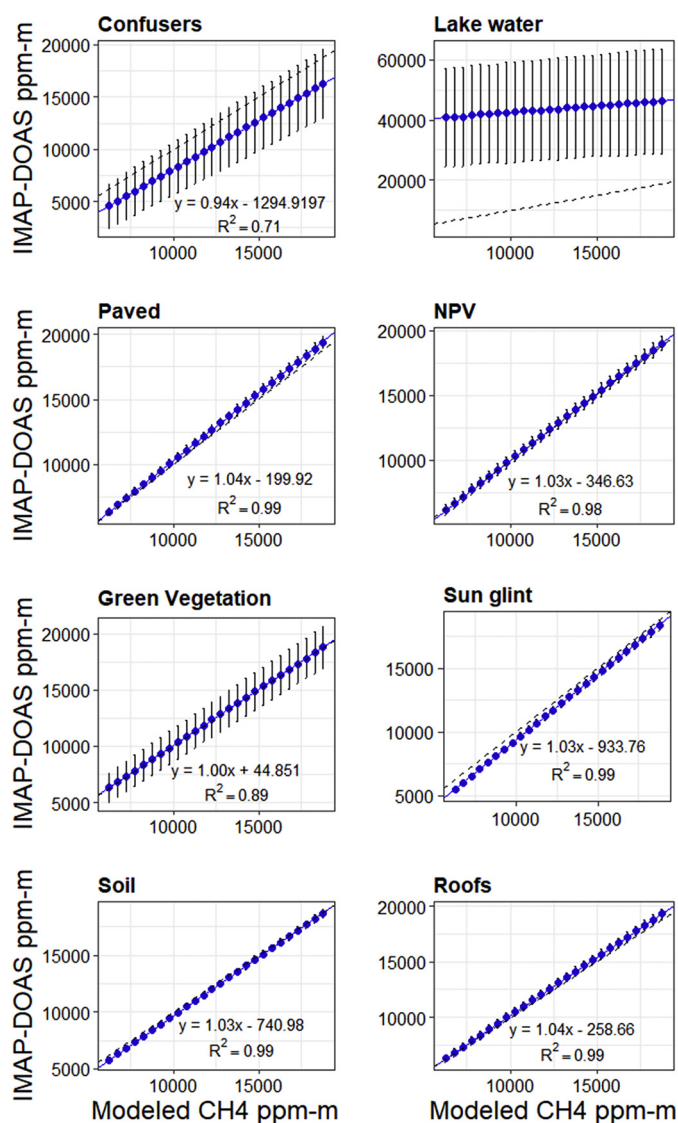


Fig. 7. The mean IMAP-DOAS retrieved concentration for each synthetic image concentration, plotted against the image concentration within each land cover class. The error bars represent one standard deviation from the mean. The dashed line represents a one-to-one relationship and the blue line is the linear regression. The slope, intercept, and r-squared for the linear model are reported for each plot except lake water. (For interpretation of the references to colour in this figure legend, the reader is referred to the web version of this article.)

painted roofs, and calcite) exhibited a large degree of error, with error increasing with methane concentration. A number of other surfaces also exhibited heteroscedastic errors, with the error tending towards overestimation with increasing methane.

In order to summarize the pattern of error, we averaged the residuals and calculated the root mean square error (RMSE) for each background spectrum (Table 4). In addition, we plotted the error for each background spectrum as box plots (Fig. 9). The Hope Lake (water), the white painted roofs, calcite, coyote brush, and golf course grass had high mean errors and had the largest RMSE. The remaining GV and confuser surfaces also had high RMSE. The soils, the paved surfaces, NPV, and roofs were the surfaces with lower mean error and lower RMSE.

Apart from the patterns associated with surface type, the results shown in Fig. 8 exhibit two characteristic error patterns: the residuals scale with the methane concentration and the results indicate slight vertical banding. We observed a greater overestimate at higher

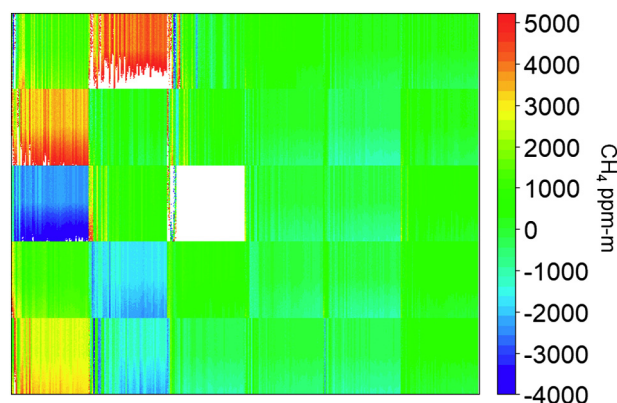


Fig. 8. The error between the synthetic image and IMAP-DOAS retrieved methane concentrations (image minus IMAP-DOAS). The white areas represent values outside of the displayed range. The all white box is lake water and the partially white box is one of the white painted roofs. See Fig. 3 for the complete configuration of the synthetic image.

methane concentrations and underestimation at low methane concentrations. These relationships between the error and the modeled methane may be due partly to the difference in how MODTRAN and IMAP-DOAS model radiance. MODTRAN accounts for multiple scattering while IMAP-DOAS does not. This means the path radiance for MODTRAN is larger than for IMAP-DOAS, and therefore an equivalent methane concentration will have a more pronounced absorption feature (Roberts et al., 2010), which is consistent with the observed IMAP-DOAS overestimates. Additionally, varying degrees of vertical banding are observed in Fig. 8. The banding results from the combined effects of the layout of the albedos in the synthetic image and the retrieval fit errors. For example, two adjacent pixels with the same concentration of modeled methane, the same surface, but with a 1% albedo difference (Fig. 3) can result in differing retrieved methane concentrations. This effect is more pronounced for certain surface types like confusers and green vegetation and less visible for bright surfaces such as soils and paved surfaces.

#### 3.4. Albedo

We also evaluated the effect of albedo on retrievals. To determine the albedo of a spectrum we used the radiance value at 2139 nm. The radiance at this wavelength is a good indicator of albedo because there are no atmospheric absorptions from any of the major greenhouse gases (Roberts et al., 2010). In addition, 2139 nm is in the SWIR, which means the radiance values represent the albedo in the region of the electromagnetic spectrum of interest. To test the influence of albedo on the IMAP-DOAS retrieved concentration, the residuals were binned by radiance level and then plotted as box plots (Fig. 10). The lowest radiance bin, with values ranging between 0 and  $0.104 \mu\text{Wcm}^{-2}\text{nm}^{-1}\text{sr}^{-1}$  at 2139 nm, had the largest spread in the residuals and the poorer results. The pixels with radiance between 0.206 and  $0.611 \mu\text{Wcm}^{-2}\text{nm}^{-1}\text{sr}^{-1}$  at 2139 nm had a much smaller range of residuals compared to the darkest pixels but still exhibited some spread. The pixels above  $0.611 \mu\text{Wcm}^{-2}\text{nm}^{-1}\text{sr}^{-1}$  had the least spread and the most accurate results. Lastly, the outlying residuals around and below 5000 and  $-2500$  ppm-m, can all be attributed to the confusers.

#### 4. Discussion

Surface type and albedo both have an effect on the methane retrieval results for the synthetic image. By isolating and quantifying the effect of different surface types, we can better understand detection limits and potential error sources of methane concentration retrievals.

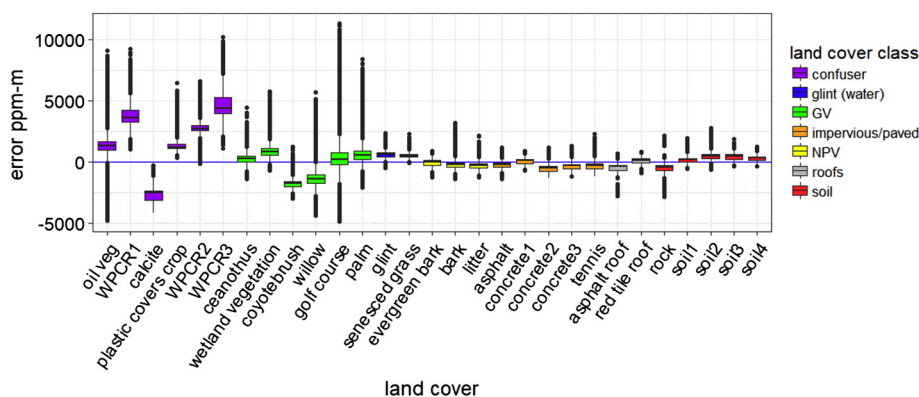


Fig. 9. Box plots of the error for every surface type. The colors, as indicated in the legend, represent the larger land cover class. Lake water is omitted. (For interpretation of the references to colour in this figure legend, the reader is referred to the web version of this article.)

Table 4

Table showing the surface name, the mean error, and root mean square error (RMSE). The surface types are organized by RMSE.

Surface type	Mean Error ppm-m	RMSE
Hope Lake water	-32,757.44	36,750.73
White painted commercial roof 3 (WPCR3)	4632.82	4748.20
White painted commercial roof 1 (WPCR1)	3799.22	3890.31
White painted commercial roof 2 (WPCR2)	2759.16	2826.87
Calcite	-2647.97	2728.81
Golf course grass	602.23	1996.17
Coyote brush (BAPI)	-1754.34	1793.47
Oil coated vegetation	1381.89	1791.71
Willow (SASP)	-1203.39	1558.20
Plastic covered crops	1379.49	1477.71
Wetland Vegetation (MARSH)	998.93	1262.71
Palm tree	689.21	1193.34
Ocean water (glint)	645.50	716.32
Rock	-429.51	657.00
Concrete parking structure 1	-488.67	608.21
Soil 4	516.57	606.86
Dead grass	545.54	593.19
Asphalt & gravel roof	-464.08	591.98
Ceanothus (CEME)	292.32	532.02
Soil 1	454.77	518.77
Tennis court	-283.93	507.79
Bark	-139.65	491.13
Concrete parking structure 2	-338.11	449.42
Needle litter	-274.18	430.17
Soil 2	318.41	393.68
Soil 3	200.05	374.79
Airport asphalt	-196.72	360.06
Evergreen bark	-41.94	283.02
Red tile roof	126.83	272.32
Concrete bridge	87.84	263.07

We found that soils, paved surfaces, roofs, and NPV generally possess high reflectance and no confusing absorption features in the SWIR and resulted in good methane retrievals. Low reflectance materials (water, green vegetation) and materials with confusing absorption features (confusers) produced large uncertainties for methane retrievals. In the following sections, we will discuss the surfaces and albedos that caused poor retrieval results, reasons for the poor results, and possible solutions.

4.1. Albedo

Albedo has a significant effect on the accuracy of the results but only for the lowest albedos. We found that surfaces (independent of surface type) with very low radiance, below  $0.10 \mu\text{Wcm}^{-2}\text{nm}^{-1}\text{sr}^{-1}$  at 2139 nm, had extremely poor results with large error. This finding is consistent with Thorpe et al. (2017) who found that dark surfaces

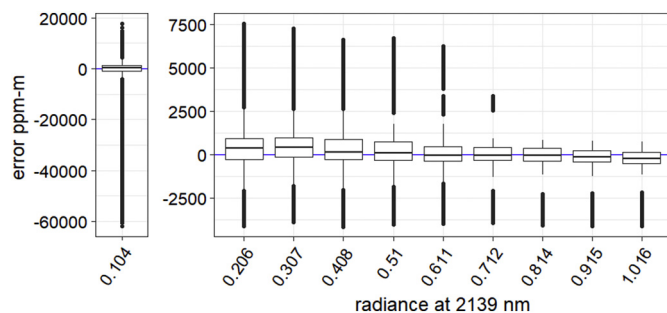
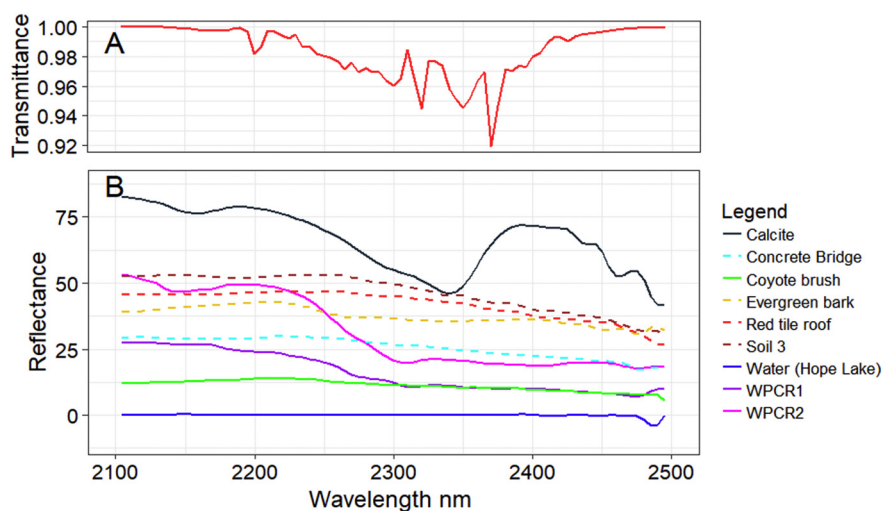


Fig. 10. The residuals between the image and IMAP-DOAS retrieved concentration (image minus IMAP-DOAS) binned by radiance at 2139 nm ( $\mu\text{Wcm}^{-2}\text{nm}^{-1}\text{sr}^{-1}$ ) and then plotted as box plots. The x-axis represents the upper level of the radiance threshold used to bin the residuals. The plot on the left has a different y-axis to accommodate the larger range in error.

resulted in anomalously high retrievals and removed spectra if there were radiance values less than  $0.01 \mu\text{Wcm}^{-2}\text{nm}^{-1}\text{sr}^{-1}$  at any band in the fitting window. M. Zhang et al. (2017), Z. Zhang et al. (2017) also examined the effects of many factors, including albedo, on a different retrieval technique and concluded that albedo was a significant factor in determining the bias of the methane concentration retrieval. In contrast, we found that the impact of albedo on retrieval accuracy was small, except at the lowest albedos. We found no linear correlation between albedo and error. For the darkest surfaces ( $0.10 \mu\text{Wcm}^{-2}\text{nm}^{-1}\text{sr}^{-1}$  and below), there is insufficient reflected radiance to discern methane absorptions. Surfaces that fell between 0.10 and  $0.60 \mu\text{Wcm}^{-2}\text{nm}^{-1}\text{sr}^{-1}$  at 2139 nm had a detectable methane signature but the error in the results was higher than for brighter surfaces. For pixels with radiance above  $0.60 \mu\text{Wcm}^{-2}\text{nm}^{-1}\text{sr}^{-1}$  at 2139 nm the range in the residuals was much lower and the column concentrations in this range are fairly accurate. In addition, all outlying error in Fig. 10 is attributed to the confusers. Although albedo affects the accuracy of the column concentration, the effect is far less significant than described in M. Zhang et al. (2017). In addition, although column concentration accuracy may be poor at low albedos, detection is still possible at all radiance values save for the lowest. As shown in Figs. 5 and 7, methane retrieval accuracy is poor for the dark lake water example however water with sunglint results in high retrieval accuracy.

4.2. Surface type

Previous studies that tested the IMAP-DOAS retrieval technique on AVIRIS Classic imagery concluded that the results were also influenced by the underlying surface (Thorpe et al., 2014). Different surface types can affect the accuracy of the IMAP-DOAS results either through the spectral shape of the material in the SWIR or with their inherent albedo.



**Fig. 11.** A) The transmittance spectra for methane calculated from MODTRAN and convolved to the AVIRIS-NG bandpass function. B) The reflectance spectra in the SWIR (2100 nm to 2500 nm) for calcite, water, the white painted roofs, soil, evergreen bark, red tile roof, coyote brush, and concrete. The solid lines represent surface types that had high amounts of error. The dashed lines represent surface types that had the lowest amount of error. (For interpretation of the references to colour in this figure legend, the reader is referred to the web version of this article.)

To explore this idea further and to better understand the error associated with surface type we looked at the spectral shape of the reflectance data in the SWIR. Fig. 11 shows the four spectra with worst accuracy, the four spectra best accuracy (accuracy is defined by the RMSE as reported in Table 4), and a GV spectrum.

#### 4.2.1. Green vegetation

Thorpe et al. (2014) noted that retrieval performance was poorer for areas dominated by green vegetation compared to areas dominated by soil. Green vegetation spectra, especially the golf course grass and coyote brush, are generally very dark in the SWIR (Fig. 11B), which was the main cause of the error. Green vegetation is not as dark as water and therefore the results are far better for green vegetation than for water. In addition, despite green vegetation having little reflectance in the SWIR, the spectral shape is relatively flat which causes improved results compared to the confuser class. Green vegetation is a very common surface type especially in natural and agricultural landscapes and therefore can make accurate quantification of methane plumes in these areas more challenging. However, green vegetation in AVIRIS-NG images can easily be classified and an estimate of uncertainty applied. In addition, future sensors with finer spectral resolution and improved gas sensitivity should have improved accuracy over vegetation (Thorpe et al., 2016a, 2016b). Lastly, although IMAP-DOAS results have some uncertainty, methane detection remains possible over vegetated surfaces.

#### 4.2.2. Confusers

The confusers had large mean error and RMSE. After lake water, the confuser class had the most error with the worst results attributed to the white painted roofs and calcite. These surfaces, although bright in the visible portion of the spectrum and part of the SWIR, have significant drops in reflectance in the methane absorption bands. In the case of the white painted roofs, the SWIR absorption is due to hydrocarbon absorptions from oil-based paints. In the case of calcite, this feature is due to the vibrational absorption bands found in carbonate minerals (Clark, 1999). These absorption features are thought to be the cause of the poor results. Other studies have also found that surfaces with strong absorption features between 2200 and 2400 nm can cause error. Thorpe et al. (2013) used a cluster-tuned matched filter to detect methane in various AVIRIS Classic scenes concluding that surfaces with hydrocarbon absorptions or any significant absorptions in the 2200 to 2500 nm window were likely to confuse the matched filter and result in a spurious signal. Our study specifically tested these types of surfaces and found that they caused error in IMAP-DOAS concentration retrieval as well but not necessarily a spurious signal. Interestingly, these surfaces did not all cause an overestimation in the methane concentration

as would be expected. Of the four surfaces with the most pronounced absorptions in the 2300 nm window, only calcite caused overestimations and the other surfaces (white painted roofs 1, 2, and 3) caused underestimations. Fig. 11 shows the spectra of calcite, white painted roof 1, and white painted roof 2. The calcite is much brighter and has a more prominent absorption versus the other white painted roofs. White painted roof 2 also has a clear absorption feature but does not have overestimation. The other white roofs, the oil coated vegetation, and the plastic covered crops also had very poor results but the cause of the error for these surfaces was due to low reflectance in the SWIR. These types of surfaces, especially the white painted roofs, are common in urban and commercial areas and can pose challenges when detecting methane plumes in these types of environments. Similar to green vegetation, these surfaces can be classified and masked out of images so as not to cause spurious signals or inaccurate results.

#### 4.2.3. Water

The largest source of error in the IMAP-DOAS results was Hope Lake. In general, water has extremely low reflectance in the SWIR (Fig. 11) and this is the source of the error in the results. Given the low reflectance over water bodies, mapping methane sources over water bodies with AVIRIS-NG will remain challenging. Despite this, methane plumes originating from water bodies, like manure lagoons and wastewater treatment plants, will still offer opportunities for plume detection and quantification as the plume moves over background surfaces with higher reflectance (Fig. 12A and B). For larger water bodies, sun glint reflected off the surface of the water can provide an excellent means of detection (Bradley et al., 2011; Roberts et al., 2010; Thorpe et al., 2014). In addition, this study concluded that results from sun glint are fairly accurate. On a global scale, wetlands are the largest natural source of atmospheric methane and are predicted to become a more important source in the future (Bridgham et al., 2013; Z. Zhang et al., 2017). This study suggests that methane detection should be possible for wetlands covered in vegetation.

#### 4.3. Comparison to real AVIRIS-NG images

These patterns are consistent with previous studies and results from IMAP-DOAS applied to real AVIRIS-NG images (Fig. 12). In Fig. 12, IMAP-DOAS methane retrievals are shown for a dairy and a coal mine ventilation shaft imaged by 2015 AVIRIS-NG flights over Bakersfield, California and the Four Corners region of the United States respectively. In both of these images, there are clear examples of the underlying surface reflectance affecting the methane retrievals. In Fig. 12B the methane plume emanates from the waste lagoons and extends southeast over the combination of buildings with metal roofs, soils, and green

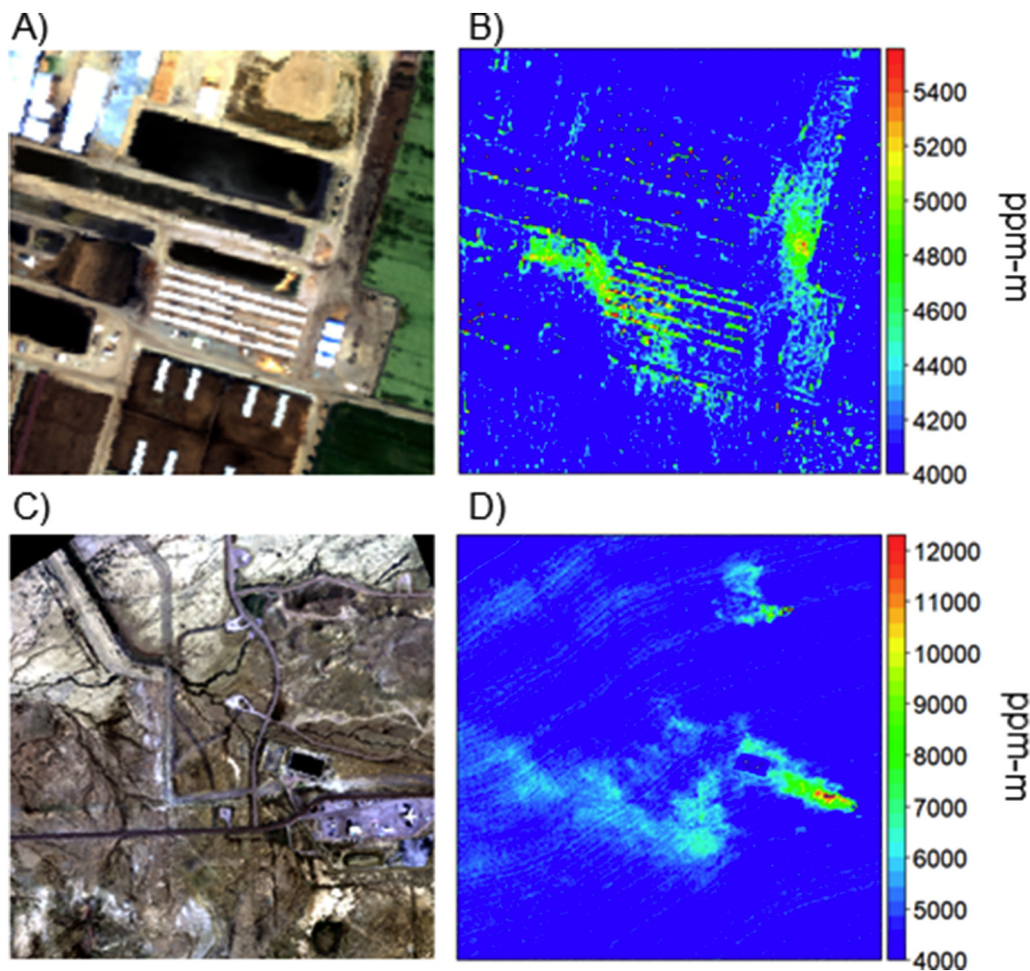


**Fig. 12.** A) True colour AVIRIS-NG image of a dairy in Bakersfield, CA April 29, 2015. The sensors height was 2.9 km resulting in a 2.6 m pixel. B) IMAP-DOAS methane retrieval for image A shows methane plumes emanating from dairy waste lagoons. C) True colour AVIRIS-NG image of coal mine ventilation shafts near the Four Corners region of the United States from April 22, 2015. The sensor height was 2.9 km resulting in a 2.7 m pixel. D) IMAP-DOAS methane retrieval for image C shows methane plumes that originate from known coal mine ventilation shafts. For all scenes north is up.

vegetation shown in Fig. 12A. The plume is most visible over the soil and roof but seems to disappear over the green vegetation due to difficulty in detecting methane over vegetation. The plume is more visible over the metallic roofs and less visible over low albedo shaded areas between the buildings. In addition, it appears that there is no methane directly over the dairy waste lagoons, due to the difficulty of methane retrieval over water. The image of a coal mine ventilation shaft (Fig. 12C) has a much larger methane plume (Fig. 12D), and the plume is clearer in this image compared to the dairy waste lagoon example. The majority of the surfaces in this image are soil, NPV, and paved surfaces, all surfaces that are ideal for retrieving methane. The one exception is the pond; the plume seems to disappear as it passes over the water due to very low radiance. The same surfaces in these images and the synthetic images cause poor detection, providing assurance that the synthetic image is accurately capturing patterns found in real imagery.

#### 4.4. Limitations and potential solutions

While this study provided an opportunity to control and test the effect of the surface properties on methane quantification, there are some limitations to this study. As mentioned previously and illustrated in Fig. 8, there was not perfect agreement between the retrieved IMAP-DOAS methane concentrations and the known concentrations from the synthetic scene. As expected, some of this was due to the underlying surface, however, some patterns in the error were unexpected and likely

due to differences in the radiative transfer calculations used in IMAP-DOAS and MODTRAN. The most notable error in the image is the slight overestimation of methane at higher concentrations. We believe this can be partly attributed to the fact that MODTRAN incorporates multiple scattering while IMAP-DOAS does not. To investigate this possibility, we ran MODTRAN without the multiple scattering component, created a small synthetic image, and ran IMAP-DOAS. We found that the overestimation decreased but not enough to explain all of the error in the results. This study primarily focused on the effect of the surface on methane detection but also determined that aerosols have a minimal influence on methane retrievals. Despite these limitations, the synthetic image remains a powerful tool to study the sensitivities of surface type and other factors on detection.

This study found that some surface types can influence the accuracy of the IMAP-DOAS results. A potential solution to account for the influence of land cover is to classify the underlying surface. In addition to the SWIR, AVIRIS-NG collects data in the visible and near infrared portion of the spectrum. This additional information can be used to classify the underlying land cover and a measure of error could be applied to each class. This could be done for classes such as vegetation and soil or for albedo classes. Additionally, a higher spectral resolution sensor will reduce sensitivity to land cover type. AVIRIS-NG has a 5 nm spectral resolution, which is well suited for mapping land cover and other surface properties. However, at 1 nm spectral resolution the spectral signatures of gases are more pronounced and have higher frequency variations compared to the surface, which should decouple

the spectral signature of the atmosphere from the surface (Thorpe et al., 2016a, 2016b). A 1 nm instrument specifically designed for gas mapping will provide increased gas sensitivity (Thorpe et al., 2016a, 2016b; Duren et al., 2017) and its performance could be tested empirically using a similar sensitivity study.

## 5. Conclusion

The synthetic AVIRIS-NG image provided an excellent framework through which we were able to test the effects of land cover and albedo on methane retrievals with the IMAP-DOAS algorithm. The synthetic image allowed us to model known methane concentrations, albedo, land cover, and other atmospheric variables. By quantifying the effects of the surface on methane retrievals, we were able to characterize the sensitivity of the IMAP-DOAS algorithm applied to AVIRIS-NG data. Overall, we found excellent agreement with the modeled methane and the IMAP-DOAS results. We found that the most accurate retrievals were over soils and paved surfaces. Conversely, we found that low albedos, below  $0.10 \mu\text{Wcm}^{-2}\text{nm}^{-1}\text{sr}^{-1}$  at 2139 nm, caused higher error in the retrieval results but above that threshold, there was significantly less error. Green vegetation had high error due to low albedo in the SWIR. Water, the darkest surface, had the most error. Confusers also had higher error due to the absorption features in the 2200–2400 nm window but not all caused a spurious signal as hypothesized. Changes in the surface can affect our ability to retrieve column concentration accurately. This means that methane plumes over water bodies will present a greater challenge and require further study and attention. Potential solutions to dealing with these challenging surfaces include using other regions of the electromagnetic spectrum to classify then flag or mask out these surfaces. Finer spectral resolution provided by future imaging spectrometers will provide greater gas sensitivity as well. The synthetic image has strength in its versatility and therefore can be modified to test the sensitivity of these future sensors or other retrieval algorithms, gas species, and land cover. Overall, the results from this study help us to understand the capabilities of the AVIRIS-NG sensor for methane retrievals and aid in understanding the limitations and uncertainty in mapping methane over large regions with variable surface types.

## Acknowledgements

The authors thank NASA HQ and Jack Kaye for funding the AVIRIS-NG flights used in this study. We would also like to thank Riley Duren for contributing to project planning and acknowledge the contributions of Robert Green, David Thompson, and the rest of the AVIRIS-NG instrument and flight teams. Portions of this research were supported the Chevron Energy Technology Company. This work was undertaken in part at the Jet Propulsion Laboratory, California Institute of Technology, under contract with NASA as well as at the University of California, Santa Barbara. The AVIRIS-NG data used in this study are available upon request at <http://avirisng.jpl.nasa.gov/> or <http://aviris.jpl.nasa.gov/>. Copyright 2017. All rights reserved.

## References

Adler-Golden, S.M., Matthew, M.W., Bernstein, L.S., Levine, R.Y., Berk, A., Richtsmeier, S.C., Acharya, P.K., Anderson, G.P., Felde, J.W., Gardner, J.A., Hoke, M.L., Jeong, L.S., Pukall, B., Ratkowski, A.J., Burke, H.K., 1999. Atmospheric correction for shortwave spectral imagery based on MODTRAN4. In: SPIE's International Symposium on Optical Science, Engineering, and Instrumentation, pp. 61–69. <http://dx.doi.org/10.1117/12.366315>.

Berk, A., Anderson, G.P., Acharya, P.K., Bernstein, L.S., Muratov, L., Lee, J., Fox, M., Adler-golden, S.M., Chetwynd, J.H., Hoke, M.L., Lockwood, R.B., Gardner, J.A., Cooley, T.W., Christoph, C., 2005. MODTRAN™ 5, a reformulated atmospheric band model with auxiliary species and practical multiple scattering options: update. SPIE 5806, 662–667. <http://dx.doi.org/10.1117/12.606026>.

Bradley, E.S., Leifer, I., Roberts, D.A., Dennison, P.E., Washburn, L., 2011. Detection of marine methane emissions with AVIRIS band ratios. Geophys. Res. Lett. 38 (n/a–n/a). <https://doi.org/10.1029/2011GL046729>.

Bridgman, S.D., Cadiello-Quiroz, H., Keller, J.K., Zhuang, Q., 2013. Methane emissions from wetlands: biogeochemical, microbial, and modeling perspectives from local to global scales. Glob. Chang. Biol. 19, 1325–1346. <http://dx.doi.org/10.1111/gcb.12131>.

Carr, S.B., 2005. The Aerosol Models in MODTRAN: Incorporating Selected Measurements from Northern Australia, Defense Science and Technology Organisation. Australian Government. DSTO-TR-1803.

Ciais, P., Sabine, C., Bala, G., Bopp, L., Brovkin, V., Canadell, J., Chhabra, A., DeFries, R., Galloway, J., Heimann, M., Jones, C., Le Quéré, C., Myneni, R.B., Piao, S., Thornton, P., 2013. Carbon and other biogeochemical cycles. In: Clim. Chang. 2013 - Phys. Sci. Basis, pp. 465–570. <http://dx.doi.org/10.1017/CBO9781107415324.015>.

Clark, R.N., 1999. Spectroscopy of rocks and minerals, and principles of spectroscopy. In: Remote Sensing for the Earth Sciences: Manual of Remote Sensing, <http://dx.doi.org/10.1111/j.1945-5100.2004.tb0079.x>.

Dennison, P.E., Thorpe, A.K., Pardyjak, E.R., Roberts, D.A., Qi, Y., Green, R.O., Bradley, E.S., Funk, C.C., 2013. High spatial resolution mapping of elevated atmospheric carbon dioxide using airborne imaging spectroscopy: radiative transfer modeling and power plant plume detection. Remote Sens. Environ. 139, 116–129. <http://dx.doi.org/10.1016/j.rse.2013.08.001>.

Duren, R., Thorpe, A., Sander, S., 2017. California Baseline Methane Survey-Interim Phase 1 Report.

Frankenberg, C., Platt, U., Wagner, T., 2004. Iterative maximum a posteriori (IMAP)-DOAS for retrieval of strongly absorbing trace gases: model studies for CH<sub>4</sub> and CO<sub>2</sub> retrieval from near infrared spectra of SCIAMACHY onboard ENVISAT. Atmos. Chem. Phys. Discuss. 4, 6067–6106. <http://dx.doi.org/10.5194/acpd-4-6067-2004>.

Frankenberg, C., Meirink, J.F., van Weele, M., Platt, U., Wagner, T., 2005. Assessing methane emissions from global space-borne observations. Science (80-) 308, 1010–1014. <http://dx.doi.org/10.1126/science.1106644>.

Frankenberg, C., Aben, I., Bergamaschi, P., Dlugokencky, E.J., Van Hees, R., Houweling, S., Van Der Meer, P., Snel, R., Tol, P., 2011. Global column-averaged methane mixing ratios from 2003 to 2009 as derived from SCIAMACHY: trends and variability. J. Geophys. Res. Atmos. 116, 1–12. <http://dx.doi.org/10.1029/2010JD014849>.

Frankenberg, C., Thorpe, A.K., Thompson, D.R., Hulley, G., Kort, E.A., Vance, N., Borchardt, J., Krings, T., Gerilowski, K., Sweeney, C., Conley, S., Bue, B.D., Aubrey, A.D., Hook, S., Green, R.O., 2016. Airborne methane remote measurements reveal heavy-tail flux distribution in Four Corners region. Proc. Natl. Acad. Sci. 113, 201605617. <http://dx.doi.org/10.1073/pnas.1605617113>.

Gao, B.C., Goetz, A.F.H., 1990. Column atmospheric water vapor retrievals from airborne imaging spectrometer data. J. Geophys. Res. - Atmos. 95, 3549–3564. <http://dx.doi.org/10.1029/JD095iD04p03549>.

Gao, B.C., Montes, M.J., Davis, C.O., Goetz, A.F.H., 2009. Atmospheric correction algorithms for hyperspectral remote sensing data of land and ocean. Remote Sens. Environ. 113, S17–S24. <http://dx.doi.org/10.1016/j.rse.2007.12.015>.

Gerilowski, K., Tretner, A., Krings, T., Buchwitz, M., Bertagnolio, P.P., Belezegov, F., Erzinger, J., Burrows, J.P., Bovensmann, H., 2011. MAMAP - a new spectrometer system for column-averaged methane and carbon dioxide observations from aircraft: instrument description and performance analysis. Atmos. Meas. Tech. 4, 215–243. <http://dx.doi.org/10.5194/amt-4-215-2011>.

Green, R.O., Eastwood, M.L., Sarture, C.M., Chrien, T.G., Aronsson, M., Chippendale, B.J., Faust, J.A., Pavri, B.E., Chovit, C.J., Solis, M., Olah, M.R., Williams, O., 1998. Imaging spectroscopy and the airborne visible/infrared imaging spectrometer (AVIRIS). Remote Sens. Environ. 65, 227–248. [http://dx.doi.org/10.1016/S0034-4257\(98\)00064-9](http://dx.doi.org/10.1016/S0034-4257(98)00064-9).

Green, R.O., Pavri, B.E., Chrien, T.G., 2003. On-orbit radiometric and spectral calibration characteristics of EO-1 hyperion derived with an underflight of AVIRIS and in situ measurements at Salar de Arizaro, Argentina. IEEE Trans. Geosci. Remote Sens. 41, 1194–1203. <http://dx.doi.org/10.1109/TGRS.2003.813204>.

Guanter, L., Segl, K., Kaufmann, H., 2009. Simulation of optical remote-sensing scenes with application to the EnMAP hyperspectral mission. IEEE Trans. Geosci. Remote Sens. 47, 2340–2351.

Hamlin, L., Green, R.O., Mouroulis, P., Eastwood, M., Wilson, D., Dudik, M., Paine, C., 2011. Imaging spectrometer science measurements for terrestrial ecology: AVIRIS and new developments. IEEE Aerosp. Conf. Proc. 1–7. <http://dx.doi.org/10.1109/AERO.2011.5747395>.

Hulley, G.C., Duren, R.M., Hopkins, F.M., Hook, S.J., Vance, N., Guillevic, P., Johnson, W.R., Eng, B.T., Mihaly, J.M., Jovanovic, V.M., Chazanoff, S.L., Staniszewski, Z.K., Kuai, L., Worden, J., Frankenberg, C., Rivera, G., Aubrey, A.D., Miller, C.E., Malakar, N.K., Sánchez Tomás, J.M., Holmes, K.T., 2016. High spatial resolution imaging of methane and other trace gases with the airborne hyperspectral thermal emission spectrometer (HyTES). Atmos. Meas. Tech. Discuss. 1–32. <http://dx.doi.org/10.5194/amt-2016-8>.

IPCC, 2016. Inventory of U.S. Greenhouse Gas Emissions and Sinks: 1990–2014. IPCC (<https://doi.org/EPA430-R-13-001>).

Jacob, D.J., Turner, A.J., Maasakkers, J.D., Sheng, J., Sun, K., Liu, X., Chance, K., Aben, I., McKeever, J., Frankenberg, C., 2016. Satellite observations of atmospheric methane and their value for quantifying methane emissions. Atmos. Chem. Phys. 16, 14371–14396. <http://dx.doi.org/10.5194/acp-16-14371-2016>.

Kirschke, S., Bousquet, P., Ciais, P., Saunois, M., Canadell, J.G., Dlugokencky, E.J., Bergamaschi, P., Bergmann, D., Blake, D.R., Bruhwiler, L., Cameron-Smith, P., Castaldi, S., Chevallier, F., Feng, L., Fraser, A., Heimann, M., Hodson, E.L., Houweling, S., Josse, B., Fraser, P.J., Krummel, P.B., Lamarque, J.-F., Langenfelds, R.L., Le Quéré, C., Naik, V., O'Doherty, S., Palmer, P.I., Pison, I., Plummer, D., Poulter, B., Prinn, R.G., Rigby, M., Ringeval, B., Santini, M., Schmidt, M., Shindell, D.T., Simpson, I.J., Spahni, R., Steele, L.P., Strode, S.A., Sudo, K., Szopa, S., van der Werf, G.R., Voulgarakis, A., van Weele, M., Weiss, R.F., Williams, J.E., Zeng, G., 2013. Three decades of global methane sources and sinks. Nat. Geosci. 6, 813–823.

- <http://dx.doi.org/10.1038/ngeo1955>.
- Kneizys, F.X., Abreu, L.W., Anderson, G.P., Chetwynd, J.H., Shettle, E., Berk, A., Bernstein, L.S., Robertson, D.C., Acharya, P., Rothman, L.S., Selby, J.E.A., Gallery, W.O., Clough, S.A., 1996. The MODTRAN 2/3 Report and LOWTRAN 7 Model.
- Kokaly, R.F., Couvillion, B.R., Holloway, J.M., Roberts, D.A., Ustin, S.L., Peterson, S.H., Khanna, S., Piazza, S.C., 2013. Remote sensing of environment spectroscopic remote sensing of the distribution and persistence of oil from the Deepwater horizon spill in Barataria Bay marshes. *Remote Sens. Environ.* 129, 210–230. <http://dx.doi.org/10.1016/j.rse.2012.10.028>.
- Krautwurst, S., Gerilowski, K., Jonsson, H., Thompson, D., Kolyer, R., Thorpe, A., Horstjann, M., Eastwood, M., Leifer, I., Vigil, S., Krings, T., Borchardt, J., Buchwitz, M., Fladeland, M., Burros, J., Bovensmann, H., 2017. Methane emissions from a Californian landfill, determined from airborne remote sensing and in-situ measurements methane emissions from a Californian landfill, determined from airborne remote sensing and in-situ measurements. *Atmos. Meas. Tech.* 3429–3452. <http://dx.doi.org/10.5194/amt-2016-391>.
- Krings, T., Gerilowski, K., Buchwitz, M., Hartmann, J., Sachs, T., Burrows, J.P., Bovensmann, H., 2013. Quantification of methane emission rates from coal mine ventilation shafts using airborne remote sensing data. *Atmos. Meas. Tech.* 151–166. <http://dx.doi.org/10.5194/amt-6-151-2013>.
- Kruse, F.a., 2004. Comparison of ATREM, ACORN, and FLAASH Atmospheric Corrections Using Low-Altitude AVIRIS Data of Boulder, CO. 13th JPL Airborne Geosci. Work. pp. 1–10.
- Lara, 2016. SB-1383 Short-lived Climate Pollutants: Methane Emissions: Dairy and Livestock: Organic Waste: Landfills. Senate, State of California.
- Matthew, M.W., Adler-Golden, S.M., Berk, A., Felde, G., Anderson, G.P., Gorodetzky, D., Paswaters, S., Shippert, M., 2002. Atmospheric correction of spectral imagery: Evaluation of the FLAASH algorithm with AVIRIS data. In: Applied Imagery Pattern Recognition Workshop, pp. 157–163. <http://dx.doi.org/10.1109/AIPR.2002.1182270>.
- Miller, C.J., 2002. Performance assessment of ACORN atmospheric correction algorithm. In: SPIE 4725, Algorithms and Technologies for Multispectral, Hyperspectral, and Ultraspectral Imagery VIII, pp. 438–449. <http://dx.doi.org/10.1117/12.478777>.
- Nisbet, E.G., Dlugokencky, E.J., Bousquet, P., 2014. Methane on the rise—again. *Science* (80-) 343, 493–495. <http://dx.doi.org/10.1126/science.1247828>.
- Nisbet, E.G., Dlugokencky, E.J., Manning, M.R., Lowry, D., Fisher, R.E., France, J.L., Michel, S.E., Miller, J.B., White, J.W.C., Vaughn, B., Bousquet, P., Pyle, J.A., Warwick, N.J., Cain, M., Brownlow, R., Zazzeri, G., Lanoisellé, M., Manning, A.C., Gloor, E., Worthy, D.E.J., Brunke, E., Labuschagne, C., Wolff, E.W., Ganesan, A.L., 2016. Rising atmospheric methane: 2007–2014 growth and isotopic shift. *Glob. Biogeochem. Cycles* 30, 1356–1370. <http://dx.doi.org/10.1002/2016GB005406>. Received.
- Platt, U., 1994. Differential optical absorption spectroscopy (DOAS). In: *Air Monitoring by Spectroscopic Techniques*. John Wiley, New York.
- Richter, R., 1996. Atmospheric correction of DAIS hyperspectral image data. *Comput. Geosci.* 22, 785–793. [http://dx.doi.org/10.1016/0098-3004\(96\)00016-7](http://dx.doi.org/10.1016/0098-3004(96)00016-7).
- Rigby, M., Montzka, S.A., Prinn, R.G., White, J.W.C., Young, D., O'Doherty, S., Lunt, M.F., Ganesan, A.L., Manning, A.J., Simmonds, P.G., Salameh, P.K., Harth, C.M., Mühle, J., Weiss, R.F., Fraser, P.J., Steele, L.P., Krummel, P.B., McCulloch, A., Park, S., 2017. Role of atmospheric oxidation in recent methane growth. *Proc. Natl. Acad. Sci.* 114, 5373–5377. <http://dx.doi.org/10.1073/pnas.1616426114>.
- Roberts, D.a., Bradley, E.S., Cheung, R., Leifer, I., Dennison, P.E., Margolis, J.S., 2010. Mapping methane emissions from a marine geological seep source using imaging spectrometry. *Remote Sens. Environ.* 114, 592–606. <http://dx.doi.org/10.1016/j.rse.2009.10.015>.
- Roberts, Dar A., Alonzo, M., Wetherley, E.B., Dudley, K.L., Dennison, P.E., 2017. Multiscale Analysis of Urban Areas Using Mixing Models. In: *Integrating Scale in Remote Sensing and GIS*, pp. 247–282. <http://dx.doi.org/10.1201/9781315373720-10>.
- Rothman, L.S., Gordon, I.E., Barbe, A., Benner, D.C., Bernath, P.F., Birk, M., Boudon, V., Brown, L.R., Campargue, A., Champion, J.P., Chance, K., Coudert, L.H., Dana, V., Devi, V.M., Fally, S., Flaud, J.M., Gamache, R.R., Goldman, A., Jacquemont, D., Kleiner, I., Lacombe, N., Lafferty, W.J., Mandin, J.Y., Massie, S.T., Mikhailenko, S.N., Miller, C.E., Moazzen-Ahmadi, N., Naumenko, O.V., Nikitin, A.V., Orphal, J., Perevalov, V.I., Perrin, A., Predoi-Cross, A., Rinsland, C.P., Rotger, M., Šimečková, M., Smith, M.A.H., Sung, K., Tashkun, S.A., Tennyson, J., Toth, R.A., Vandaele, A.C., Vander Auwera, J., 2009. The HITRAN 2008 molecular spectroscopic database. *J. Quant. Spectrosc. Radiat. Transf.* 110, 533–572. <http://dx.doi.org/10.1016/j.jqsrt.2009.02.013>.
- Schaefer, H., Mikaloff Fletcher, S.E., Veidt, C., Lassey, K.R., Brailsford, G.W., Bromley, T.M., Dlugokencky, E.J., Michel, S.E., Miller, J.B., Levin, I., Lowe, D.C., Martin, R.J., Vaughn, B.H., White, J.W.C., 2016. A 21st century shift from fossil-fuel to biogenic methane emissions indicated by 13CH4. *Science* (80-) 351. <http://dx.doi.org/10.1126/science.aad2705>.
- Schwietzke, S., Sherwood, O.A., Bruhwiler, L.M.P., Miller, J.B., Etiope, G., Dlugokencky, E.J., Michel, S.E., Arling, V.A., Vaughn, B.H., White, J.W.C., Tans, P.P., 2016. Upward revision of global fossil fuel methane emissions based on isotope database. *Nature* 538, 88–91. <http://dx.doi.org/10.1038/nature19797>.
- Strow, L.L., Hannon, S.E., De Souza-Machado, S., Motteler, H.E., Tobin, D., 2003. An overview of the AIRS radiative transfer model. *IEEE Trans. Geosci. Remote Sens.* 41, 303–313. <http://dx.doi.org/10.1109/TGRS.2002.808244>.
- Thompson, D.R., Leifer, I., Bovensmann, H., Eastwood, M., Fladeland, M., Frankenberg, C., Gerilowski, K., 2015. Real-time remote detection and measurement for airborne imaging spectroscopy: a case study with methane. *Atmos. Meas. Tech.* 8, 4383–4397. <http://dx.doi.org/10.5194/amt-8-4383-2015>.
- Thompson, D.R., Thorpe, A.K., Frankenberg, C., Green, R.O., Duren, R., Guanter, L., Hollstein, A., Middleton, E., Ong, L., Ungar, S., 2016. Space-based remote imaging spectroscopy of the Aliso canyon CH4 super-emitter. *Geophys. Res. Lett.* <http://dx.doi.org/10.1002/2016GL069079>.
- Thorpe, A.K., Roberts, D.a., Bradley, E.S., Funk, C.C., Dennison, P.E., Leifer, I., 2013. High resolution mapping of methane emissions from marine and terrestrial sources using a cluster-tuned matched filter technique and imaging spectrometry. *Remote Sens. Environ.* 134, 305–318. <http://dx.doi.org/10.1016/j.rse.2013.03.018>.
- Thorpe, A.K., Frankenberg, C., Roberts, D.A., 2014. Retrieval techniques for airborne imaging of methane concentrations using high spatial and moderate spectral resolution: application to AVIRIS. *Atmos. Meas. Tech.* 7, 491–506. <http://dx.doi.org/10.5194/amt-7-491-2014>.
- Thorpe, A.K., Frankenberg, C., Aubrey, A.D., Roberts, D.A., Nottrott, A.A., Rahn, T.A., Sauer, J.A., Dubey, M.K., Costigan, K.R., Arata, C., Steffke, A.M., Hills, S., Haselwimmer, C., Charlesworth, D., Funk, C.C., Green, R.O., Lundeen, S.R., Boardman, J.W., Eastwood, M.L., Sarture, C.M., Nolte, S.H., McCubbin, I.B., Thompson, D.R., McFadden, J.P., 2016a. Mapping methane concentrations from a controlled release experiment using the next generation airborne visible/infrared imaging spectrometer (AVIRIS-NG). *Remote Sens. Environ.* 179, 104–115. <http://dx.doi.org/10.1016/j.rse.2016.03.032>.
- Thorpe, A.K., Frankenberg, C., Green, R.O., David, R., Aubrey, A.D., Mouroulis, P., Eastwood, M.L., 2016b. The Airborne Methane Plume Spectrometer (AMPS): Quantitative imaging of methane plumes in real time. In: *IEEE Aerospace Conference*.
- Thorpe, A.K., Frankenberg, C., Thompson, D.R., Duren, R.M., Aubrey, A.D., Bue, B., Green, R.O., Gerilowski, K., Krings, T., Borchardt, J., Kort, E.A., Conley, S., Roberts, D.A., Dennison, P.E., 2017. Airborne retrievals of methane, carbon dioxide, and water vapor concentrations at high spatial resolution: Application to AVIRIS-NG. *Atmos. Meas. Tech.* 10, 3833–3850.
- Thurmond, Williams, 2015. AB 1496 Methane Emissions. Assembly, State of California.
- Tratt, D.M., Buckland, K.N., Hall, J.L., Johnson, P.D., Keim, E.R., Leifer, I., Westberg, K., Young, S.J., 2014. Remote sensing of environment airborne visualization and quantification of discrete methane sources in the environment. *Remote Sens. Environ.* 154, 74–88. <http://dx.doi.org/10.1016/j.rse.2014.08.011>.
- Turner, A.J., Frankenberg, C., Wennberg, P.O., Jacob, D.J., 2017. Ambiguity in the causes for decadal trends in atmospheric methane and hydroxyl. *Proc. Natl. Acad. Sci.* 114, 5367–5372. <http://dx.doi.org/10.1073/pnas.1616020114>.
- Yokota, T., Yoshida, Y., Eguchi, N., Ota, Y., Tanaka, T., Watanabe, H., Maksyutov, S., 2009. Global concentrations of CO2 and CH4 retrieved from GOSAT: first preliminary results. *Sola* 5, 160–163. <http://dx.doi.org/10.2151/sola.2009-041>.
- Zhang, M., Leifer, I., Hu, C., 2017a. Challenges in methane column retrievals from AVIRIS-NG imagery over spectrally cluttered surfaces: a sensitivity analysis. *Remote Sens. Environ.* 193, 835. <http://dx.doi.org/10.1016/j.rse.2017.08.035>.
- Zhang, Z., Zimmermann, N.E., Stenke, A., Li, X., Hodson, E.L., Zhu, G., Huang, C., Poulter, B., 2017b. Emerging role of wetland methane emissions in driving 21st century climate change. *Proc. Natl. Acad. Sci.* 201618765. <http://dx.doi.org/10.1073/pnas.1618765114>.